journal

J. Am. Ceram. Soc., **81** [9] 2394–404 (1998)

Contact Damage and Strength Degradation in Brittle/Quasi-Plastic Silicon Nitride Bilayers

Kee Sung Lee,† Seung Kun Lee,*,‡ and Brian R. Lawn*

Materials Science and Engineering Laboratory, National Institute of Standards and Technology, Gaithersburg, Maryland 20899

Do Kyung Kim*

Department of Materials Science and Engineering, Korea Advanced Institute of Science and Technology, Yusong, Taejon 305-701, Korea

A study is made of the damage resistance of silicon nitride bilayers consisting of a hard overlayer (coating) on a soft underlayer (substrate). The two layers are fabricated with different starting powders, to provide distinctive elongate-grain microstructures, and are cosintered, to provide strong interfacial bonding and thus to minimize subsequent delamination. Contact testing with spherical indenters is used to characterize the damage response. The elastic-plastic mismatch between the layers is sufficiently high as to produce distinctive damage modes in the two layers: predominantly cone cracking in the coating, and quasi-plasticity in the substrate. However, the mismatch is also sufficiently low as to preclude secondary transverse cracks of the kind observed in other bilayer systems to initiate immediately beneath the contact at the coating/substrate interface and propagate upward within the coating. The dominant damage mode shifts from coating fracture to substrate quasi-plasticity with increasing contact load and decreasing coating thickness. Significantly, the presence of the soft underlayer inhibits growth of the coating cone cracks as the latter approach and intersect the interface. The underlayer also substantially diminishes strength losses from the contact-induced damage, especially in bilayers with thinner coatings. The implication is that bilayer structures with thin, hard coatings can preserve benefits from the inherent toughness of soft substrate materials, and at the same time afford surface protection (high wear resistance) to the underlayer.

I. Introduction

OVER the last decade there has been a drive to improve the toughness of silicon nitride (Si_3N_4) and other silicon-based ceramics via *in situ* growth of long, elongate grains.[1–12] In Hertzian contacts with spherical indenters these enlarged and elongated microstructures produce diffuse energy-absorbing subsurface quasi-plastic zones, consisting of individual, grain-localized microfailures (''shear faults''[13]), instead of conventional surface-initiated cone cracks.[14–18] At moderate contact loads this quasi-plastic damage has a comparatively minor degrading effect on strength in ensuing flexure or tension.[19,20] However, at higher contact loads or numbers of repeat cycles the microfailures tend to coalesce within the damage zone, with consequent accelerated strength loss and material removal.[21] Accordingly, quasi-plastic damage can have a highly adverse effect on resistance to fatigue[21] and wear[22] (although it can also promote machinability[23]). Improvement in mechanical properties from *in situ* tailoring of microstructures is not universal.

The search for ceramic structures with superior property combinations has led to a novel concept of layered homogeneous/heterogeneous microstructures with relatively hard surfaces (coatings) on soft underlayers (substrates).[24,25] A critical element of this concept is the incorporation of interlayer elastic–plastic mismatch, so as to partition energy from the contact loading system into competing fracture and quasi-plasticity modes, with the principal intent of containing the former mode without unduly promoting the latter. Another critical element is incorporation of strong rather than weak interlayer interfaces, so as to avoid delamination—the aim is to suppress rather than to deflect cone (or other) cracks that originate in the coating. The existence of any compression stresses in the coating from thermal expansion mismatch with the substrate will further inhibit the extension of any such cracks.[26,27] In principle, such a composite layer system should exhibit both high wear resistance and high toughness, with reduced susceptibility to strength degradation from damage accumulation.

In a recent study we investigated these critical elements in Si_3N_4 bilayers with uncommonly large elastic–plastic mismatch,[28] achieved by incorporating boron nitride (BN) platelets into the sublayer structure.[29,30] In Hertzian contact tests these bilayers showed confined transverse cracking in the coatings, along with extensive yield in the substrates. In thinner coatings with higher mismatch the soft substrate allowed the hard coating to ''flex'' beneath the contact, further enhancing the transverse cracking. In these cases some of the transverse cracks initiated from the coating/substrate interface rather than from the coating top surface, at relatively low loads. The cracks were highly stabilized, requiring exceptionally high loads to drive them upward through the coating, thereby enabling the crack population to multiply. It was clear that any such proliferation of cracks, while contributing to damage tolerance, could ultimately compromise the structural integrity of the coating, especially if the bilayer were to be subjected to high or repeat loading. It would seem that there are upper limits to the useful range of mismatch in these structures.

In the present work we investigate an analogous Si_3N_4 bilayer system, but with much smaller elastic–plastic mismatch, in an attempt to retain the advantages of the layer concept without inducing excessive transverse cracking. Bilayers with

G. M. Pharr—contributing editor

Manuscript No. 190682. Received September 22, 1997; approved December 19, 1997.

Supported by the U.S. Air Force Office of Scientific Research.

*Member, Amercian Ceramic Society.

†Graduate student at the Department of Materials Science and Engineering, Korea Advanced Institute of Science and Technology, Yusong, Taejon 305-701, Korea.

‡Now at Advanced Material Technology Division, Technical Center, Caterpillar Inc., Mossville, Illinois 61552.

relatively brittle and quasi-plastic Si_3N_4 components are fabricated, but without addition of a softening agent in the substrate. The two Si_3N_4 layers are fabricated from different starting powders, at specified layer thicknesses, but are cosintered to produce a strong adjoining interface. Contacts with spheres are used to induce controlled damage patterns into the layered specimens and ceramographic sectioning techniques used to examine these patterns. Bend tests on damaged bar specimens are carried out to investigate the role of the different damage modes on strength degradation.

We shall show that whereas the Si_3N_4 coating layers are still subject to cone cracking, they show no deleterious interface-initiated transverse cracking. Quasi-plastic damage is more limited than in the previous BN-doped substrate structures,[28] but nevertheless appears to play an important role in restricting extension of the surface ring cracks within the coating. Strengths of contact-damaged bilayers are enhanced relative to those of the (comparatively weak) coating material, tending at small coating thicknesses to those of the (comparatively strong) substrate material. The results suggest the prospect of designing layer structures for both high toughness and high wear resistance.

II. Experimental Procedure

(1) Powders and Processing

Two different Si_3N_4 powders were selected for preparation of the bilayers. The starting powder for the coating layers was α-Si_3N_4 of mean particle size 1.0 μm (UBE-SN-E3, Ube Industries, Tokyo, Japan), with additives 5 wt% Y_2O_3 (Fine Grade, H. C. Starck GmbH, Goslar, Germany), 2 wt% Al_2O_3 (AKP 50, Sumitomo Chemical Co. Ltd., Tokyo, Japan), and 1 wt% MgO (High Purity, Baikowski Co., NC). The powder for the substrate layers was α-Si_3N_4 of average particle size 0.3 μm (UBE-SN-E10, Ube Industries, Tokyo, Japan), with the same sintering additives. Previously,[18] these two final batches were designated **AC** (α-coarse) and **AF** (α-fine), according to Si_3N_4 starting powder—here, we use the simpler designation **C** (coating) and **S** (substrate).

A Si_3N_4 powder batch with 30 vol% BN softening additive from another preceding study[28] was used as a comparison substrate—this material is here designated **S30.**

The powder batches were each mixed in isopropyl alcohol for 24 h in a planetary ball-mill using zirconia balls in a polypropylene container, to form a slurry. After drying, the softly agglomerated powder was crushed and sieved through a 60-mesh screen. The powders were cold-pressed in a graphite mold of 50 mm diameter to form green state bilayers of coating thickness 1 mm and substrate thickness 3–4 mm. The composite structure was hot-pressed at 1700°C at a pressure of 30 MPa in nitrogen for 1 h.[18] Some monolithic samples of each powder mix were prepared for control studies.

Surfaces of some specimens were polished to 1 μm finish, plasma etched, gold coated, and examined by scanning electron microscopy (SEM) to reveal the microstructures.

(2) Mechanical Testing

Fired bilayers and monolithic controls were cut into bars for mechanical testing. Routine measurements of Young's modulus, using a sonic method, and hardness, using Vickers indentations (load/projected area), were carried out on representative monolithic specimens. For the bilayers, the **C** (coating) structure was placed on the top, and the **S** (substrate) structure on the bottom. The top surfaces of the bars were then ground and polished to 1 μm diamond paste finish to produce coating thicknesses d_c = 20–600 μm. Additional Vickers indentations were made on polished sides of representative bilayer specimens to evaluate any differential thermal expansion stresses in the coatings, from radial crack measurements.[31] Some specimens were cut in half and the opposing surfaces polished and glued together to produce ''bonded-interface'' specimens[18,32,33] for investigation of subsurface damage in indentation tests. Other specimens were edge chamfered and polished for strength testing.

Hertzian indentations were made on the top surfaces of bilayer specimens, as well as on control monolith specimens, using WC spheres of radius r = 1.98 mm at loads up to P = 4000 N, in air. On as-polished specimens, rows of indentations were made at small load intervals to determine the critical loads P_Y and P_C for first incidence of yield and cracking. Application of a gold coat greatly enhanced detection of the initial damage in Nomarski illumination.[17] For the cracking an acoustic detector placed on the top surface adjacent to the indenter was a useful adjunct.[14,17] On bonded-interface specimens the indentations were made in rows symmetrically across the interface traces at the top surfaces. After separating the indented specimen halves in solvent and coating with gold, Nomarski illumination was used to view the subsurface damage.

Four-point flexure tests were run on bilayer and monolith bar specimens (25 mm × 4 mm × 3 mm, inner span 10 mm, outer span 20 mm) after indentation. The indentation sites were covered with a drop of silicone oil before testing and centered on the tensile side of the bend fixture. The bars were then broken in fast fracture (<10 ms) to avoid the influence of moisture (''inert'' strengths). ''Effective strengths'' were calculated from beam theory, using the conventional relation

$$\sigma_F = 3Ql/4wd^2 \quad (1)$$

with l the moment span, w the bar width, d the composite bilayer half-thickness, and Q the breaking load. Later, in Section III(3), we shall take into account the influence of thermal expansion mismatch (Appendix A) and interlayer modulus mismatch (Appendix B) on strengths evaluated from fracture mechanics considerations (Appendix C).

The broken specimens were examined in Nomarski illumination and scanning electron microscopy to locate the sources and modes of failure, i.e., from cone cracks or quasi-plastic zones.[19] Control strength tests on unindented specimens were made to measure baseline ''natural'' strengths.

III. Results

(1) Characterization of Silicon Nitride Layer Materials

Figure 1 shows bimodal microstructures for the two materials.[18] Common to both microstructures at the high end of the bimodal distribution are enlarged, elongated β-phase grains of length ≈5 μm and width ≈1.0 μm. In the **C** material (Fig. 1(a)) the volume fraction of this high-end grain component is relatively small (≈23 vol%)—the bulk of the microstructure consists of finer, equiaxed α-phase grains of diameter ≈1.2 μm (≈77 vol%). In the **S** material (Fig. 1(b)) the volume fraction of the high-end grain component is increased (≈40 vol%)—in this case the bulk of the microstructure consists of finer elongate β-phase grains of length ≈2 μm and width ≈0.5 μm (≈60 vol%).

Young's modulus and hardness are shown for **C** Si_3N_4 and **S** Si_3N_4 in the bar chart of Fig. 2, along with comparison values for **S30** Si_3N_4. The **C** material is slightly stiffer and harder than **S,** which in turn is very much stiffer and harder than **S30.** Note that the relative differences are considerably greater in the hardness than in the modulus, corresponding to greater plastic than elastic mismatch. For reference, bearing grade Si_3N_4 typically falls somewhere between the **C** and **S** materials—e.g., measurements on commercially available NBD200 (Norton/TRW Ceramics, Northboro, MA) give modulus 320 GPa and hardness 17.5 GPa.

The bar chart in Fig. 3 shows critical loads P_Y and P_C for first incidence of yield and cracking beneath Hertzian contacts in the same monolith material set. The critical load P_Y falls off strongly through the sequence **C–S–S30,**[18,28] commensurate

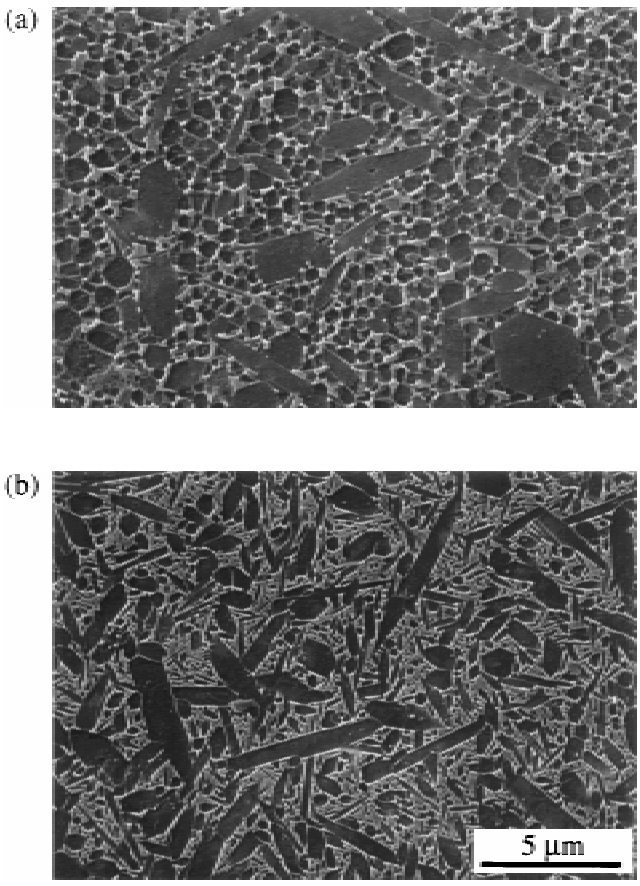

Fig. 1. SEM of Si_3N_4 materials used in bilayer: (a) **C** (coating), (b) **S** (substrate). Surfaces plasma etched (10 min in CF_4 and O_2).

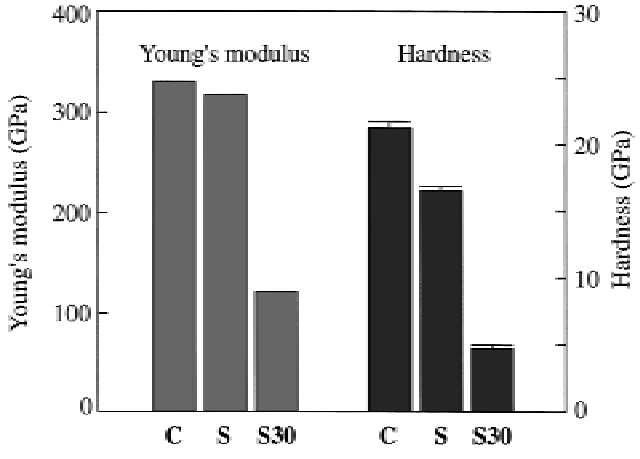

Fig. 2. Bar chart showing Young's modulus and indentation hardness of **C, S,** and **S30** (Si_3N_4–30 vol% BN). Data from Ref. 18.

with the hardness trend in Fig. 2. Conversely, P_C increases strongly, such that whereas full cone cracks are generated in **C**, only shallow surface ring cracks appear in **S**,[18] and no ring cracking is observed at all in **S30** over the load range.[28] Note that for **C** the values of P_Y and P_C are comparable, suggesting a relatively balanced competition between yield and fracture in this material.

Figure 4 plots biaxial compression stresses σ_R associated with differential thermal expansion between **C** and **S** layers, as a function of coating thickness d_c. The data are evaluations from radial crack measurements on the coating sections; the

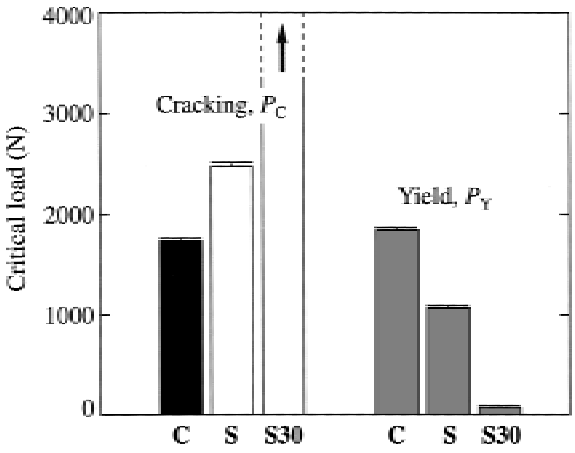

Fig. 3. Bar chart showing critical loads for onset of yield, P_Y, and cracking, P_C, of **C, S,** and **S30** Si_3N_4, tests in air. For P_C data, unfilled bar indicates only surface ring crack (as distinct from fully developed cone); absence of bar for **S30** indicates absence of any ring cracking at all. Data from Refs. 18 and 28.

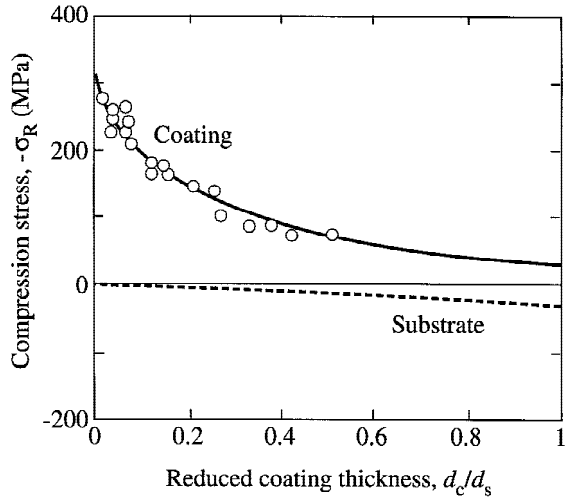

Fig. 4. Compression stresses in **C** layers from thermal expansion mismatch with **S** substrates, as a function of reduced coating thickness d_c/d_s, for constant bilayer thickness $d_c + d_s = 3000$ μm. Data from Vickers indentations (plotted here with compression stress on positive axis). Solid curve is fitted theoretical function through coating data; dashed curve is corresponding function for substrate (Appendix A).

solid curve is a theoretical fit to these data. Details of the data evaluations and fit are described in Appendix A.

(2) Contact Damage in Bilayers

Figure 5 compares bonded-interface section views of damage sites in bulk and bilayer Si_3N_4 structures, from indentations with a WC sphere of radius $r = 1.98$ mm at load $P = 3000$ N made on the top surface. In the bulk **C** specimen (Fig. 5(a)) we observe the developed cone crack (a faint trace of the subsurface quasi-plasticity zone below the contact becomes apparent in this material at high magnification). In the bilayer **C/S** specimen (Fig. 5(b)) the cone crack is substantially shallower and is contained wholly within the **C** layer (thickness $d_c = 180$ μm). The quasi-plasticity zone is now more intense and extends into the softer **S** underlayer. In a **C/S30** bilayer specimen (Fig. 5(c)), included here from the earlier study[28] for comparison as a case of extreme mismatch, the coating ($d_c = 250$ μm) contains an array of transverse cracks, including both cone cracks initiated from the top surface and upward-extending ''inverted

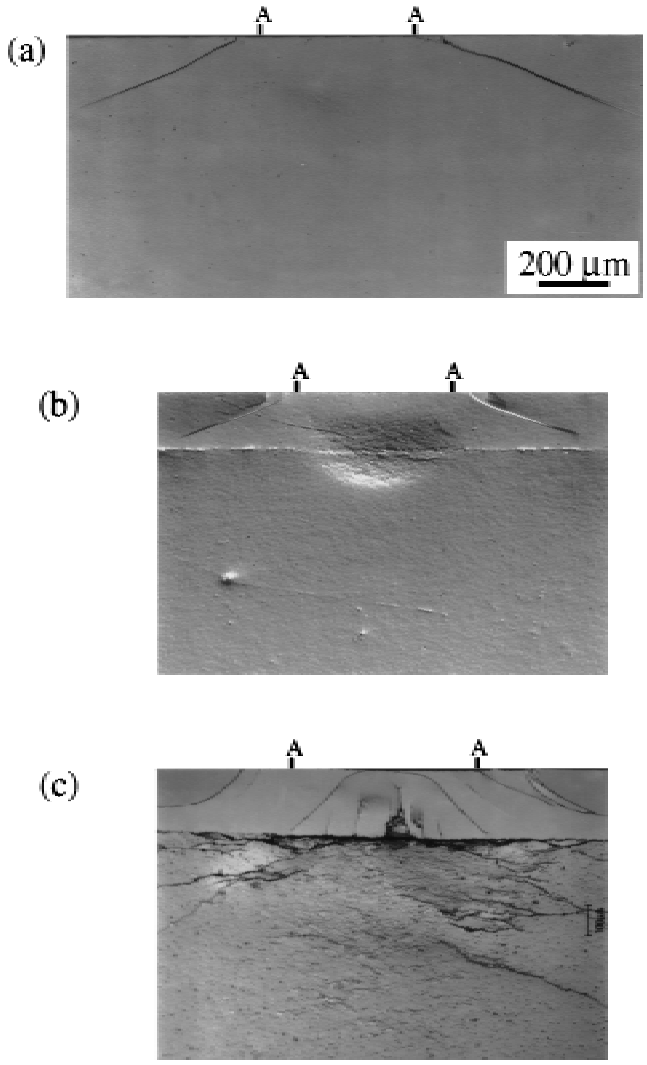

Fig. 5. Side views of Hertzian contact damage in Si_3N_4 configurations, using WC sphere of radius $r = 1.98$ mm at load $P = 3000$ N: (a) **C** monolith, showing fully developed cone crack with modest subsurface quasi-plasticity; (b) **C/S** bilayer, $d = 180$ μm, showing shortened cone crack in **C** layer and enhanced quasi-plasticity extending into **S** layer; (c) **C/S30** bilayer, $d_c = 250$ μm, showing proliferation of transverse cracks in **C** and extensive yield in **S30** (from Ref. 28). Nomarski optical micrographs of bonded-interface specimens. Contact diameter AA indicated. Interlayer interface revealed by relief polishing.

cone'' cracks initiated at the interlayer interface.[28] Yield and associated microcrack damage in the **S30** sublayer is now extensive, and some interfacial delamination is evident. It is apparent that incorporation of a soft underlayer can inhibit fracture if the mismatch with the coating material is small, but can enhance fracture if the mismatch is large. Note that the load $P = 3000$ N used in Fig. 5 exceeds both P_Y and P_C for the monolithic **C** material (Fig. 3), consistent with the appearance of both yield and cracking in the coating layer.

Now consider results for **C/S** bilayers in greater detail, taking the effects of contact load and coating thickness in turn:

(A) Effect of Contact Load: Micrographs of Hertzian contact damage in **C/S** Si_3N_4 bilayers with **C** coating thickness $d_c = 180$ μm (±10 μm) are shown in Fig. 6 over a sequence of contact loads. At $P = 2000$ N (Fig. 6(a)) a cone crack has initiated and there is a limited quasi-plasticity zone, both confined to the coating. At higher loads $P = 2500$ N (Fig. 6(b)), $P = 3000$ N (Fig. 6(c)), and $P = 3500$ N (Fig. 6(d)) both cracking and quasi-plasticity zone expand. However, whereas the cone crack remains confined to the coating, the quasi-plasticity now extends into the substrate. With further loading to $P = 4000$ N (Fig. 6(e)) the cone crack penetrates the interlayer interface, but remains inhibited (note that a second cone crack has now appeared), while the quasi-plasticity expands and intensifies within the substrate. The sequence in Fig. 6 suggests that the response is dominated by coating fracture at low load and by substrate plasticity at high load.[24]

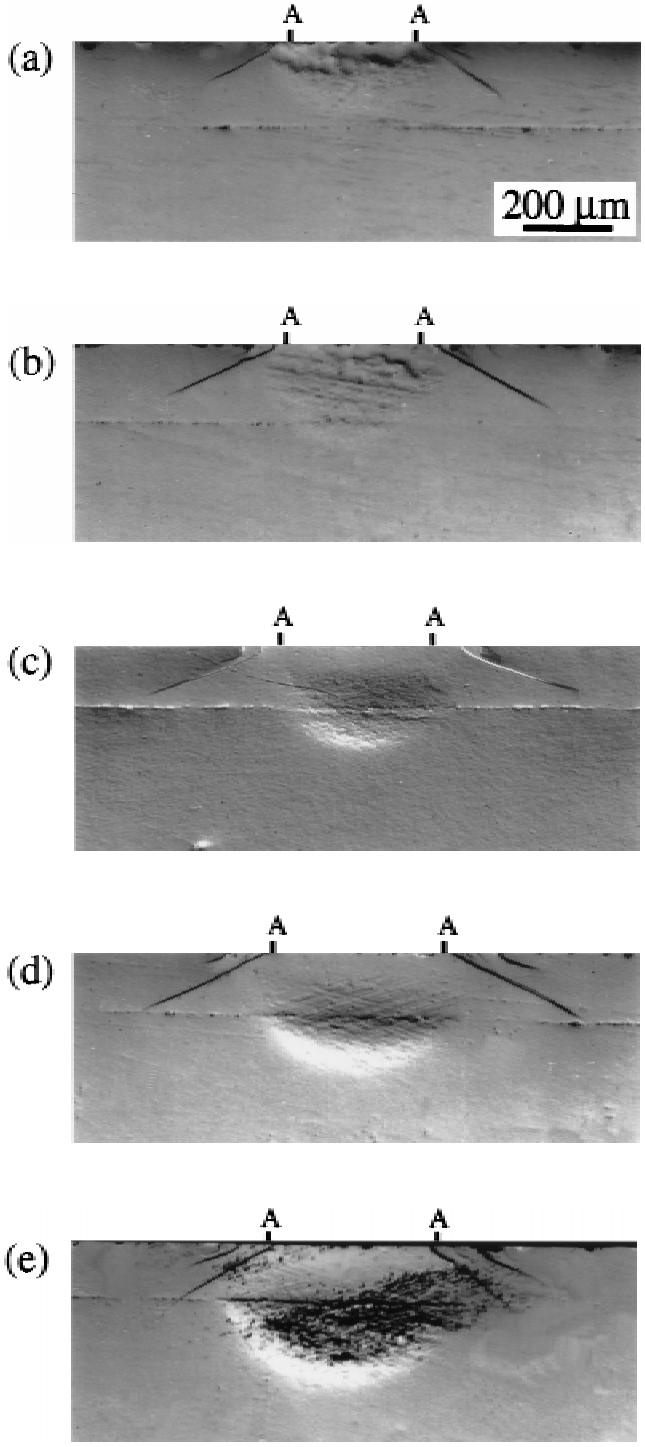

Fig. 6. Side views of Hertzian contact damage in **C/S** Si_3N_4 bilayers, fixed coating thickness $d_c = 180 \pm 10$ μm, using WC sphere radius $r = 1.98$ mm: at loads (a) $P = 2000$ N, (b) 2500 N, (c) 3000 N, (d) 3500 N, (e) 4000 N. Nomarski optical micrographs of bonded-interface specimens. Contact diameter AA indicated.

Measured cone crack depths h below the top surface are plotted as a function of load P in Fig. 7 for both the **C/S** bilayer and the **C** monolith, for the coating thickness $d_c = 180$ μm

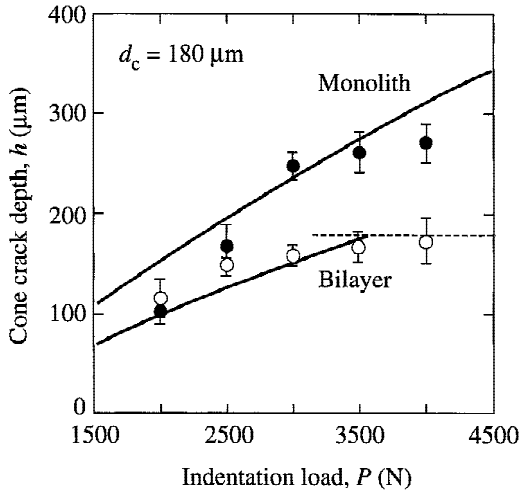

Fig. 7. Plot of cone crack depth as function of indentation load for **C/S** Si_3N_4 bilayers (open symbols), at fixed coating thickness d_c = 180 μm (horizontal dashed line), WC sphere r = 1.98 mm. Data for **C** monolith (closed symbols) provide baseline reference. Solid curves represent fracture mechanics best-fit to monolith data and ensuing prediction for bilayer.

indicated by the horizontal shaded line. The solid curves are representations of fracture mechanics relations for pennylike cone cracks in layers subjected to superposed uniform stresses σ_R, described in detail in Appendix C. The curve through the monolith data is a best-fit to these relations in the limit σ_R = 0—this fit is used to ''calibrate'' essential crack-geometry parameters. The curve through the bilayer data is an ensuing prediction for coatings with $\sigma_R = -190$ MPa (d_c = 180 μm in Fig. 4), using the calibrated crack-geometry parameters. (Note that this latter curve remains valid only while the cone crack remains embedded in the coating, i.e., $h < d_c$ in Fig. 7.) The presence of the expansion mismatch stress would appear to account for the bulk of the data shift between bilayer and monolith, notwithstanding the scatter in data.

(B) Effect of Coating Thickness: The sequence of micrographs of Hertzian contact damage in **C/S** Si_3N_4 bilayers at fixed contact load P = 3000 N in Fig. 8 illustrates the effect of coating thickness on the damage pattern. For a relatively thick coating layer, d_c = 600 μm (Fig. 8(a)), both cone crack and quasi-plasticity zone are wholly contained within the coating. As the coating is made thinner, d_c = 400 μm (Fig. 8(b)), both crack and plasticity zone remain contained within the coating, with attendant slight diminution in the cone crack depth. At d_c = 180 μm (Fig. 8(c)), the cracks are still contained, but the yield zone penetrates into the substrate. In the thinnest coatings, d_c = 80 μm (Fig. 8(d)) and d_c = 40 μm (Fig. 8(e)) the cracks, although still highly constrained, occasionally penetrate into the substrate (e.g., right side of Fig. 8(d)); the quasi-plasticity zone is now contained largely within the substrate. The sequence in Fig. 8 suggests that the response is dominated by coating fracture at high thicknesses, and by substrate plasticity at low thicknesses.

Figure 9 plots cone crack depth h as a function of coating thickness d_c, at fixed load P = 3000 N. The horizontal dashed line denotes the cone crack depth in the **C** monolith and the inclined dashed line denotes the locus $h = d_c$ for which the cone crack just intersects the **C/S** interface. The plot demonstrates quantitatively the extent to which the interface increasingly constrains the cone crack as the coating layer becomes thinner. At small coating thicknesses, $d_c < 180$ μm, some limited penetration into the substrate does occur, but the constraining influence nevertheless persists down to the smallest coating thicknesses. The solid curve is the fracture mechanics prediction for cone cracks in coatings with nonzero $\sigma_R(d_c)$, using the calibrated crack-geometry parameters from the monolith data

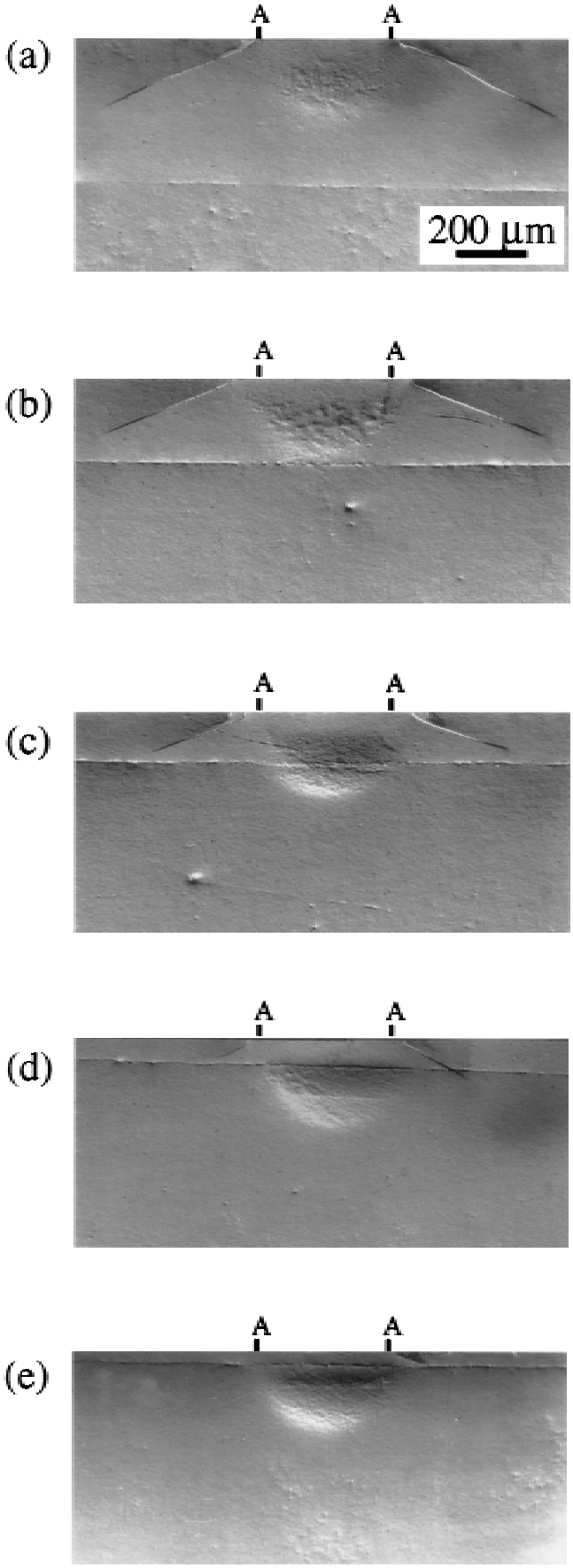

Fig. 8. Side views of Hertzian contact damage in **C/S** Si_3N_4 bilayers, at fixed load P = 3000 N using WC sphere radius r = 1.98 mm: at coating thicknesses (a) d_c = 400 μm, (b) 250 μm, (c) 180 μm, (d) 80 μm, (e) 40 μm. Nomarski optical micrographs of bonded-interface specimens. Contact diameter AA indicated.

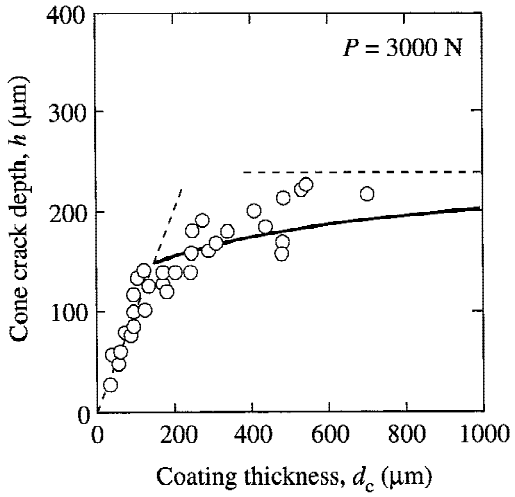

Fig. 9. Plot of cone crack depth as function of coating thickness for **C/S** Si_3N_4 bilayers (open symbols), WC sphere $r = 1.98$ mm, at fixed load $P = 3000$ N. Solid curve is fracture mechanics prediction. Inclined dashed line indicates configurations $h = d_c$ for which cracks just intersect the interface; horizontal dashed line indicates crack depth in **C** monolith.

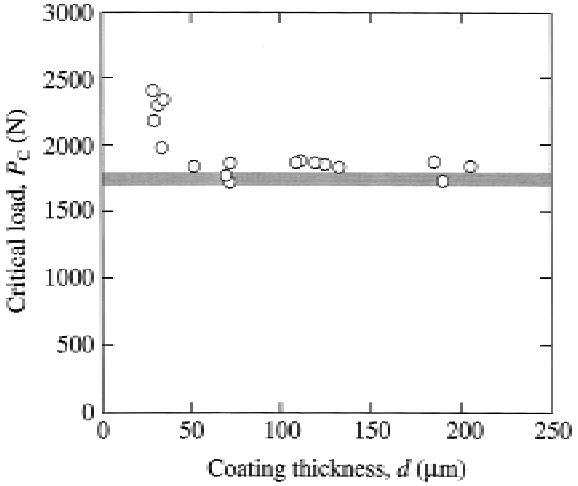

Fig. 11. Critical loads P_C for cone crack initiation as a function of coating thickness d_c for **C/S** Si_3N_4 bilayers, WC sphere radius $r = 1.98$ mm. Horizontal dashed line indicates P_C for the coating monolith.

in Fig. 7 (Appendix C). (Once more, this curve remains valid only while the cone crack remains embedded in the coating, i.e., $h < d_c$). Again, the presence of expansion mismatch stresses would appear to account for the data trends, within the scatter.

On those occasions when the coating cone cracks do penetrate into the substrate the crack paths undergo only minor deflections at the **C/S** interface, without delamination. Figure 10 is an example, for an indentation in a thin coating, $d_c = 40$ μm, at high load, $P = 4000$ N. Note the continuity of the grain structure across the interface in this figure, confirming a strong interface.

While the presence of the substrate clearly has an important

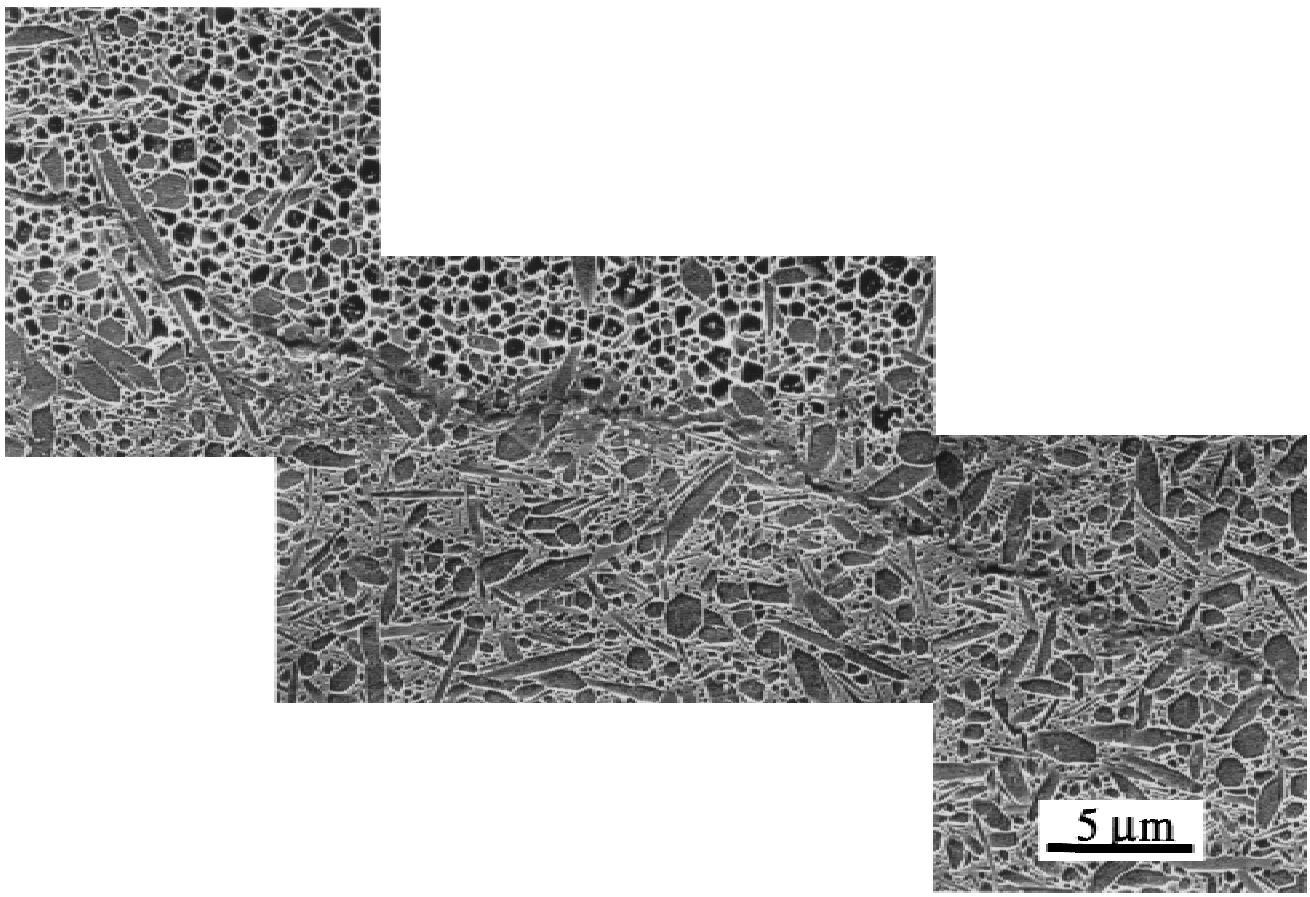

Fig. 10. Side view of Hertzian cone crack near **C/S** interface in Si_3N_4 bilayer of coating thickness $d_c = 40$ μm, at load $P = 4000$ N using WC sphere radius $r = 1.98$ mm. Note crack penetration from coating (top) to substrate (bottom) without delamination. Scanning electron micrograph.

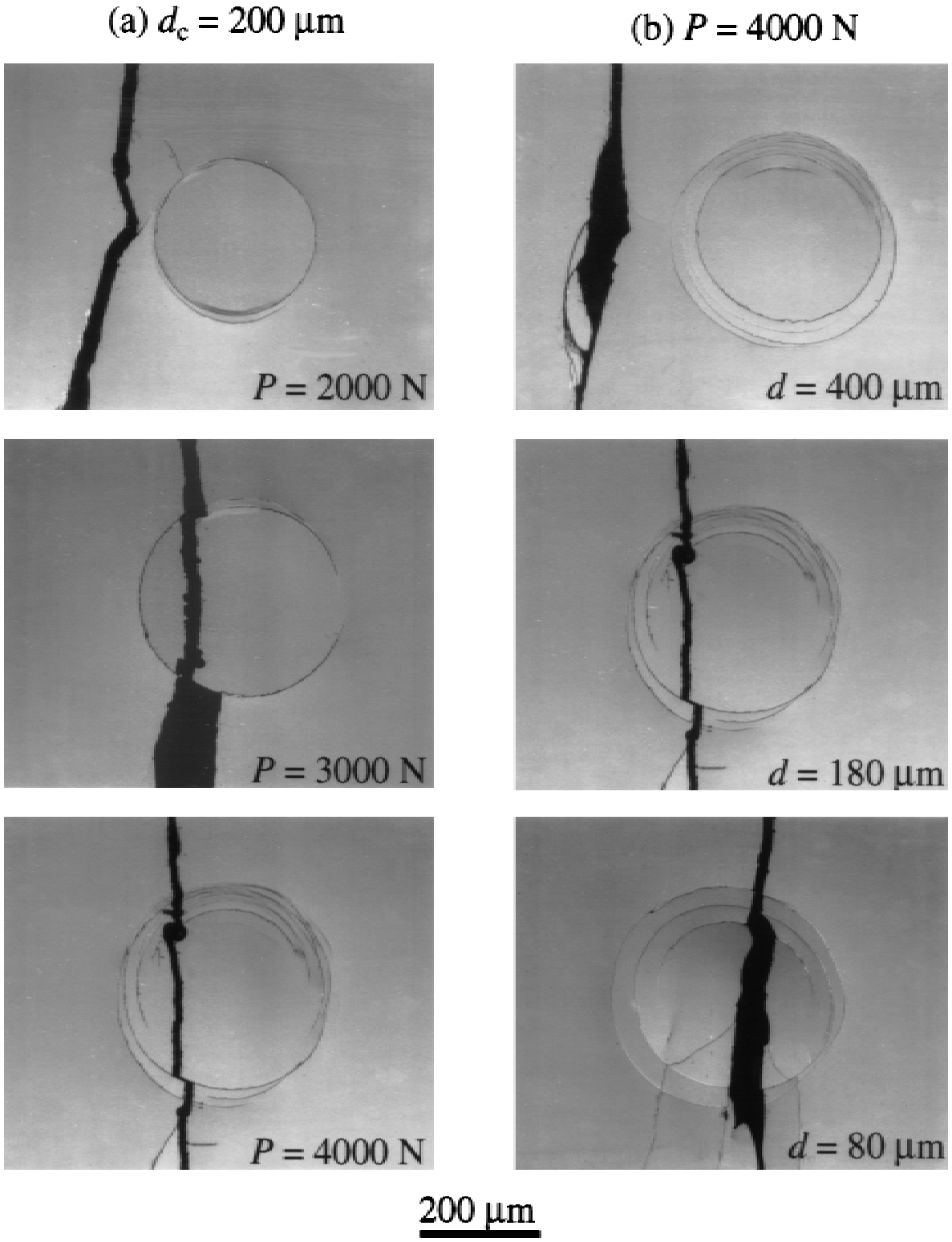

Fig. 12. Failure origins in bend specimens of **C/S** Si_3N_4 bilayers, for contacts with WC sphere radius r = 1.98 mm: (a) d_c = 200 μm, at P = 2000, 3000, and 4000 N; (b) P = 4000 N, at d_c = 400, 200, and 80 μm. Failure paths tangential to ring crack indicate brittle failure in **C** layer, through ring crack indicate quasi-plastic failure in **S** substrate. Tensile axis horizontal.

influence on the cone crack *size*, it does not appear to be a strong factor in the critical load for cone crack *initiation*. A plot of P_C as a function of coating thickness d_c is presented in Fig. 11. The values are relatively unchanged from those for the **C** monolith (shaded band—see Fig. 3) at thicknesses down to $d_c \approx 40$ μm, below which P_C increases.

(3) Strength Degradation

Figure 12 shows failure origins on broken bilayer strength-test specimens containing indentations from WC spheres of radius r = 1.98 mm, for two sets of conditions: (a) for fixed coating thickness d_c = 200 μm, at increasing (postcritical) loads; (b) for fixed load P = 4000 N, at decreasing thick-

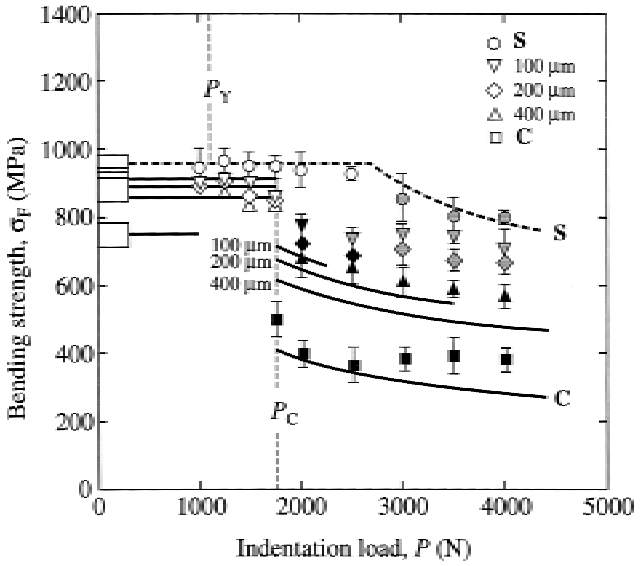

Fig. 13. Strength degradation of **C/S** Si_3N_4 bilayers, plus **C** and **S** monoliths, for contacts with WC sphere radius $r = 1.98$ mm. Data plotted as a function of indentation load P, for coating thicknesses indicated. Open symbols indicate breaks away from indentation sites, gray symbols failures from quasi-plastic zones, black symbols failures from cone cracks. Boxes at left axis denote strengths of unindented specimens. Vertical dashed lines indicate values of P_Y for **S,** P_C for **C.** Solid curves are theoretical predictions assuming failure from cone cracks at $P > P_C$ and from microstructural flaws at $P < P_C$, for **C** monoliths (lowest curve) and **C/S** bilayers at 400, 200, and 100 μm (upper three curves, truncated at loads and coating thicknesses where cones penetrate into substrate). Dashed curve is empirical fit to **S** data.[18]

nesses. Characteristic failure modes are indicated by peripheral fracture paths tangent to the ring cracks at low P and high d_c, and by more centralized fracture paths through the ring cracks at high P and low d_c. In conjunction with Figs. 6 and 8, we may associate the first kind of failure with cone cracks in the coating (brittle mode) and the second kind with yield zones in the substrate (quasi-plastic mode).[28]

Experimental data for the strength σ_F of **C/S** Si_3N_4 bilayers as a function of contact load P are plotted in Fig. 13, for **C** layer thicknesses $d_c = 100$, 200, and 400 μm, as well as for the **C** and **S** monoliths. Data points are from indented specimens: open symbols indicate breaks away from indentation sites, gray symbols failures from substrate quasi-plastic zones, and black symbols failures from coating cone cracks. Different regions of load dependence are apparent in the strength data: at $P < P_C$ (vertical dashed line), no significant load dependence; at $P = P_C$, abrupt falloff; at $P > P_C$, slowly continuing falloff, with failures first from cone cracks and later, at higher loads and thinner coatings, from quasi-plastic zones. The effects of coating thickness are manifest: whereas at $P < P_C$ the strength values for the bilayers differ little either from each other or from the **C** or **S** bounds, at $P > P_C$ the data shift strongly upward from the **C** lower bound toward the **S** upper bound.

Fracture mechanics analyses of strength degradation for failures from cone cracks have been developed for monolithic materials,[34] including Si_3N_4.[19] Analogous computation of strengths in bilayer systems is complicated by the additional stress terms associated with mismatch between coating and substrate: from mismatch in thermal expansion coefficients during initial cooling[26,27] (Appendix A); and from mismatch in elastic moduli during subsequent flexure (Appendix B). For a flaw of characteristic dimension c with negligible residual contact field, the strength under such conditions may be written (Appendix C)

$$\sigma_F = (T_0/\psi_\alpha c^{1/2} - \sigma_R)/k \qquad (2)$$

with ψ_α a crack geometry coefficient for Hertzian cones inclined at angle α to the top surface, T_0 the toughness (assumed single-valued), σ_R an expansion mismatch stress (Appendix A), and k an elastic mismatch coefficient (Appendix B). The solid curves in Fig. 13 are *a priori* predictions of $\sigma_F(P)$ for failure from cone cracks, using Eq. (2) in conjunction with appropriate expressions for the cone crack depth h ($= c \sin \alpha$) as a function of load P, for each of the coating thicknesses d_c represented. These curves truncate at the loads corresponding to cone crack penetration into the substrate, i.e., at depth $h = d_c$. The predictions appear to account for the broad data shifts for those specimens that fail from cone cracks in Fig. 13, although the absolute predictions lie outside the range of data scatter.

Once the cone cracks approach and penetrate into the tough substrate, failure occurs from the subsurface quasi-plasticity zones. Corresponding analyses of strength degradation from grain-localized ''shear faults'' within quasi-plasticity zones are being developed.[34] These are even more complex than the analyses for cone cracks, because of additional driving forces associated with residual local stress fields at the slipped shear faults.[34,35]

IV. Discussion

In this study we have confirmed that microstructural tailoring can have a vital influence on the damage tolerance of bilayer structures. An essential element in the tailoring is avoidance of a weak interface at the interlayer junction, in the present instance by cosintering the starting powders. We have focused specifically on Si_3N_4 bilayers with harder coatings on softer substrates, with modest mismatch. In contacts with spheres the coatings show mainly cone cracking and the substrates mainly quasi-plasticity (Figs. 5, 6, and 8). Which mode dominates the composite damage depends on the contact load and coating thickness: cone cracking tends to dominate at low loads and thick overlayers; conversely, quasi-plasticity tends to dominate at high loads and thin overlayers. The failure mode of the bilayer structure in flexure strength tests (Fig. 12) is also sensitive to these factors: coating cracks provide the sources of failure at low loads and thick coatings, and quasi-plasticity zones the sources at high loads and thin coatings—delamination is not observed in these modest-mismatch bilayers.

These results suggest some prescriptions for layer design using adjoining materials with modest elastic–plastic mismatch. In the case of the Si_3N_4 bilayers studied here the important microstructural elements are fine α-phase grains in the coating microstructure, to improve hardness, and coarse, elongate β grains in the substrate microstructure, to enhance quasi-plasticity. For these kinds of structures it may be concluded that thin, harder (and more brittle) wear-resistant coatings on softer (and tougher) underlayers may usefully provide surface protection without seriously compromising strength properties. Where possible, the layers should be cofired to minimize the risk of delamination failure.

The typical damage pattern in the present Si_3N_4 bilayer system provides a marked contrast to that in analogous bilayer substrates containing BN platelets (cf. Figs. 5(b) and (c)).[28] In the latter system the elastic–plastic mismatch is much greater (Fig. 2), and the yield in the substrate consequently much more extensive, allowing the coating to undergo a substantial component of ''flexure'' on the soft support beneath the contact. Such flexure leads to intense concentration of tensile stresses within the coating at the coating/substrate interface,[36] with consequent generation of upward-extending transverse cracks[37,38] at relatively low loads. While such cracks tend to be highly stable, they also tend to proliferate within the coating, compromising the subsequent integrity of the bilayer. In the present Si_3N_4 system the mismatch is too small to allow significant buildup of coating tensile stresses at the substrate interface, restricting the fracture to conventional cone cracking. At the

same time, as we have seen, the mismatch is sufficient to promote failures from subsurface quasi-plasticity zones at high loads and thin coatings.

The data in Figs. 11 and 13 warrant further comment, because collectively they characterize the contact loading conditions under which bilayer structures with modest (but nonzero) mismatch may operate without incurring intolerable strength losses from contact damage. Figure 11 indicates that the critical contact load P_C for cone crack initiation is largely insensitive to coating thickness d_c in the present bilayer system, at least down to $d_c \approx 50$ μm (relative to the sphere radius 1.98 mm used in our experiments). On the other hand, Fig. 13 indicates that the ensuing abrupt strength decrement at $P = P_C$ is very much sensitive to d_c. This behavior is consistent with St. Venant's principle in elasticity theory:[39] in the near field outside the contact circle at the top coating surface, where the cone cracks initiate during indentation, the maximum tensile stresses are very high and are relatively unaffected by the presence of moderate thermal expansion stresses or yield in the remote substrate; in the far field below the contact, where the cone cracks propagate (Fig. 8), the tensile stresses are much more strongly influenced by these extraneous factors, especially at higher P and smaller d_c.[28] In the thinner coatings the higher thermal expansion stresses and increased subsurface yield ultimately suppress cone fracture, leading to the change in mode of failure observed in Fig. 12.

A complete understanding of this latter kind of quasi-plasticity-initiated failure in layered structures is currently under study.

APPENDIX A

Differential Thermal Expansion Stresses in Bilayer Coatings

In-plane biaxial stresses σ_R from **C/S** coating/substrate thermal expansion mismatch are measured from the lengths of radial cracks at the vertical corners of Vickers indentations on coating sections (Fig. A1). The stress-intensity factor K for Vickers radial cracks of half-length c is given by[31]

$$K = \chi_V P/c^{3/2} + \psi_V \sigma_R c^{1/2} = K_{IC} = T_0 \quad \text{(A-1)}$$

with $\chi_V = 0.066$ an indentation coefficient for fine-grain Si_3N_4,[17] $\psi_V = 0.77$ a geometrical radial crack coefficient,[40] and T_0 the toughness (assumed single-valued[17]). Measurements from comparative Vickers indentations in the **C** monolith ($\sigma_R = 0$) enable the determination $T_0 = 4.2$ MPa·m$^{1/2}$.

The stresses σ_R can also be calculated from a force balance relation for bilayers with thermal expansion mismatch between coating (c) and substrate (s):[27]

$$\sigma_R = (\alpha_c - \alpha_s)E_c\Delta T/\{(1 - \nu_c) + (1 - \nu_s)(E_c/E_s)(2d_c/d_s)\} \quad \text{(A-2)}$$

where α is the thermal expansion coefficient, E is Young's modulus, ν is Poisson's ratio, and d_c is layer thickness. The solid curve through the coating data in Fig. 4 is a best fit of Eq. (A-2) to the data, with the adjustments $(\alpha_c - \alpha_s)E_c\Delta T/(1 - \nu_c) = -311$ MPa and $E_c(1 - \nu_s)/E_s(1 - \nu_c) = 4.92$. Inserting $\alpha_c = 4.16 \times 10^{-6}$ °C^{-1} and $\alpha_s = 4.62 \times 10^{-6}$ °C^{-1} (dilatometer measurements, N_2 atmosphere, 25–1000°C), $E_c = 335$ GPa and $\nu_c = 0.29$ (sonic wave measurements), the fit yields the following estimates: $\Delta T = 1430$°C, which would appear to be a little higher than the temperature range over which stresses no longer relax; and $E_s/(1 - \nu_s) = 95.9$ GPa, which is substantially lower than the measured value 315 GPa/$(1 - \nu_s) = 431$ GPa (sonic wave measurements).

In view of the numerical discrepancies between Eqs. (1) and (2), the values of σ_R in Fig. 4 should be regarded as no more than first approximation estimates.

Equivalent stresses in the substrate can be similarly evaluated by inverting the subscripts c and s in Eq. (A-2).

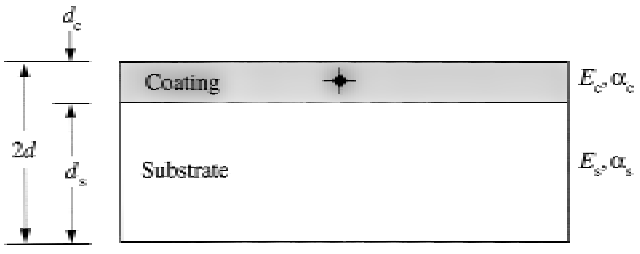

Fig. A1. Coating/substrate bilayer, with elastic and thermal expansion mismatch. Vickers indentations are used to evaluate thermal expansion mismatch stresses in coating.

APPENDIX B

Bending Stresses in Layer Structures with Different Elastic Moduli

Consider a bilayer consisting of two rectangular bars of same width w, but of different thickness d_c and d_s and modulus E_c and E_s (c = coating, s = substrate), perfectly bonded at the common interface (Fig. B1). The composite bar is subjected to bending, with layer c on the tensile side and layer s on the compression side. Although the strain distribution across the bilayer is linear and continuous, the stress distribution suffers a discontinuity at the interface.

We are specifically concerned with the maximum tensile stresses in the coating at the top surface, σ_c, and in the substrate at the interlayer interface, σ_s. The stresses of interest in four-point bending are related to the effective strength σ_F in Eq. (1) by

$$\sigma = (3Pl/4wd^2)k = k\sigma_F \quad \text{(B-1)}$$

where k is a dimensionless factor (unity for $d_c = d_s$, $E_c = E_s$). The stress distributions can be determined in a straightforward manner from thin beam theory.[41] Let us write

$$\delta = d_c/d_s \quad \text{(B-2}a\text{)}$$

$$\varepsilon = E_c/E_s \quad \text{(B-2}b\text{)}$$

For the tensile stress in the top surface of the coating (layer 1), we obtain

$$k_c = \varepsilon(2 + 1/\delta + \varepsilon\delta)/\{3\varepsilon + (1 + 1/\delta^3)(1 + \varepsilon\delta)/(1 + 1/\delta)^2\} \quad \text{(B-3)}$$

For the tensile stress in the substrate at the interlayer interface we have

$$k_s = (1/\delta - \varepsilon\delta)/\{3\varepsilon + (1 + 1/\delta^3)(1 + \varepsilon\delta)/(1 + 1/\delta)^2\} \quad \text{(B-4)}$$

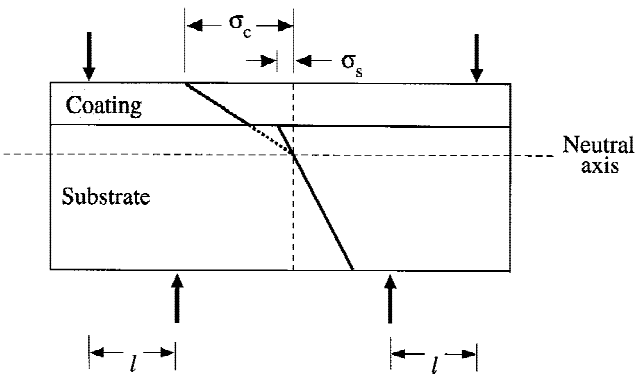

Fig. B1. Four-point bending of bilayer, generating maximum stress σ_c in the coating and σ_s in the substrate.

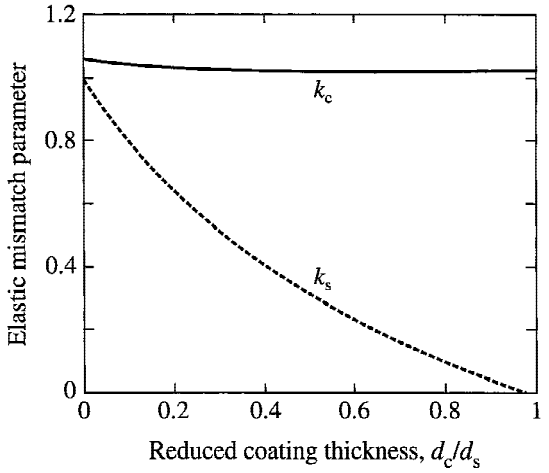

Fig. B2. Plot of elastic mismatch parameters k_c and k_s for coating and substrate in flexure, as function of reduced coating thickness d_c/d_s.

The coefficients k_c and k_s are plotted as a function of δ in Fig. B2, for $\varepsilon = E_c/E_s = 335/315 = 1.06$ appropriate to our Si_3N_4 bilayer system.

APPENDIX C

Calculation of Cone Crack Depths and Strengths for Bilayers

For the Si_3N_4 bilayers that fail from cone cracks in the coating we use a fracture mechanics analysis developed elsewhere.[19,34]

The cone crack depth is determined from the following geometrical relations, from Fig. C1:

$$h = c \sin \alpha \tag{C-1}$$

$$c = C - R_0/\cos\alpha \tag{C-2}$$

with α the cone angle, C the face length of a virtual conical surface with tip located above the indented surface, and R_0 the radius of the surface ring crack. To a first approximation, the cone cracks at contact load P satisfy an equilibrium stress-intensity relation for penny-like cracks[17]

$$K = \chi_H P/C^{3/2} + \Psi_0(\sigma_R \sin^2 \alpha)c^{1/2} = T_0 \tag{C-3}$$

with χ_H and ψ_0 Hertzian coefficients for straight-ahead cone extension, and T_0 the toughness (again assumed single-valued). This latter relation incorporates allowance for the action of the (resolved) stress σ_R on the cone crack response (Appendix A).

Equations (C-1) to (C-3) form the basis for the computations of cone crack depths in Figs. 7 and 9, plotted in those two figures as the solid curves. We take $\alpha = 25°$ and $R_0 = 238$ μm from direct measurements (e.g., Figs. 6 and 8), along with $T_0 = 4.2$ MPa·m$^{1/2}$ (Appendix A). (Actually, α and R_0 may be expected to vary with σ_R, and hence with coating thickness, but any such variations are slight enough to be masked by the data scatter in our Si_3N_4 system.) The value of the parameter ψ_α is simply that for mode I straight-ahead extension, $\psi_0 = \pi^{1/2} = 1.77$.[42] The parameter $\chi_H = 0.0311$ is ''calibrated'' from a best fit of Eqs. (C-1) to (C-3) to the $h(P)$ data for *monolithic* **C** Si_3N_4 in Fig. 7 ($\sigma_R = 0$). The corresponding curves for the *bilayer* data in Figs. 7 and 9 are predictions, using appropriate values of $\sigma_R(d_c)$ from Appendix A in Eqs. (C-1) to (C-3). (Note that this analysis is valid only while the cone crack remains embedded in the coating, i.e., $h < d_c$ in Fig. 9.)

Strength degradation functions may be determined from conventional fracture mechanics for failure from cone cracks in flexure.[34,42] Above the critical load P_C for cone initiation, the stress-intensity factor for equilibrium cone cracks in an applied field σ_A and superposed field σ_R is

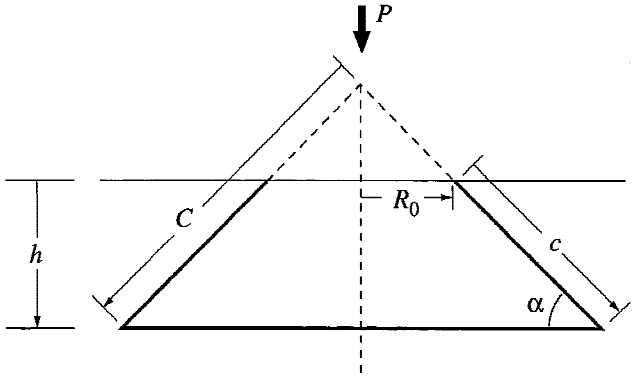

Fig. C1. Cone crack geometry.

$$K = \psi_\alpha \sigma c^{1/2} = T_0 \tag{C-4}$$

where $\sigma = \sigma_A + \sigma_R = k_c\sigma_F$. Failure then occurs spontaneously from the cone base according to the strength relation

$$\sigma_F = (T_0/\psi_\alpha c^{1/2} - \sigma_R)/k_c \tag{C-5}$$

with ψ_α a crack geometry coefficient for Hertzian cones at angle α. This relation again makes allowance for the presence of thermal expansion mismatch stresses σ_R (Appendix A) and for stress modifications associated with the elastic mismatch parameter k_c in flexure (Appendix B). At failure, the cone crack reinitiates unstably in predominantly tensile mode from its base, at some angle to α, thereby determining ψ_α. Below the critical load P_C, the ψ term in Eq. (C-5) is governed by the geometry of preexisting natural flaws, independent of P.

The functions $\sigma_F(P)$ calculated from Eq. (C-5), in conjunction with Eqs. (C-2) and (C-3), are included as the solid curves at $P > P_C$ in Fig. 13. For these calculations, ψ_α is determined from a previous analysis of crack reinitiation from the cone crack base, from which $\psi_\alpha = 0.037\alpha = 0.93$ approximately for $\alpha = 25°$.[34] Appropriate values of $k(d_c)$ are computed from Appendix B. (Note again that this analysis is valid only while the cone crack remains embedded in the coating.)

Acknowledgment: We thank T.-J. Chuang for providing the solution in Appendix B.

References

[1]C.-W. Li and J. Yamanis, ''Super-Tough Silicon Nitride with *R*-Curve Behavior,'' *Ceram. Eng. Sci. Proc.*, **10** [7–8] 632–45 (1989).

[2]T. Kawashima, H. Okamoto, H. Yamamoto, and A. Kitamura, ''Grain Size Dependence of the Fracture Toughness of Silicon Nitrides Ceramics,'' *J. Ceram. Soc. Jpn.*, **99**, 1–4 (1991).

[3]C.-W. Li, D.-J. Lee, and S.-C. Lui, ''*R*-Curve Behavior and Strength of *In-Situ* Reinforced Silicon Nitride with Different Microstructures,'' *J. Am. Ceram. Soc.*, **75** [7] 1777–85 (1992).

[4]N. Hirosaki and Y. Akimune, ''Effect of Grain Growth of β-Silicon Nitride on Strength, Weibull Modulus, and Fracture Toughness,'' *J. Am. Ceram. Soc.*, **76** [7] 1892–94 (1993).

[5]A. J. Pyzik and D. R. Beaman, ''Microstructure and Properties of Self-Reinforced Silicon Nitride,'' *J. Am. Ceram. Soc.*, **76** [11] 2737–44 (1993).

[6]P. F. Becher, S. L. Hwang, H. T. Lin, and T. N. Tiegs, ''Microstructural Contributions to the Fracture Resistance of Silicon Nitride Ceramics''; pp. 87–100 in *Tailoring of Mechanical Properties of Si_3N_4*. Edited by M. J. Hoffmann and G. Petzow. Kluwer Academic Publishers, Dordrecht, Netherlands, 1994.

[7]M. J. Hoffmann, ''Analysis of Microstructural Development and Mechanical Properties of Si_3N_4''; pp. 59–72 in *Tailoring of Mechanical Properties of Si_3N_4*. Edited by M. J. Hoffmann and G. Petzow. Kluwer Academic Publishers, Dordrecht, Netherlands, 1994.

[8]N. P. Padture, ''*In Situ* Toughened Silicon Carbide,'' *J. Am. Ceram. Soc.*, **77** [2] 519–23 (1994).

[9]S. K. Lee and C. H. Kim, ''Effects of α-SiC versus β-SiC Starting Powders on Microstructure and Fracture-Toughness of SiC Sintered with Al_2O_3-Y_2O_3 Additives,'' *J. Am. Ceram. Soc.*, **77** [6] 1655–58 (1994).

[10]C.-W. Li, S.-C. Lui, and J. Goldacker, ''Relation Between Strength, Microstructure, and Grain-Bridging Characteristics in *In-Situ* Reinforced Silicon Nitride,'' *J. Am. Ceram. Soc.*, **78** [2] 449–59 (1995).

[11]P. Sajgalik, J. Dusza, and M. J. Hoffmann, ''Relationship between Microstructure, Toughness Mechanisms, and Fracture Toughness of Reinforced Silicon Nitride Ceramics,'' *J. Am. Ceram. Soc.*, **78** [10] 2619–24 (1995).

[12]J. J. Cao, W. J. Moberly Chan, L. C. DeJonghe, C. J. Gilbert, and R. O. Ritchie, ''*In Situ* Toughened Silicon Carbide with Al–B–C Additives,'' *J. Am. Ceram. Soc.*, **79** [2] 461–69 (1996).

[13]B. R. Lawn, N. P. Padture, H. Cai, and F. Guiberteau, ''Making Ceramics 'Ductile','' *Science*, **263**, 1114–16 (1994).

[14]N. P. Padture and B. R. Lawn, ''Toughness Properties of a Silicon Carbide with an *In-Situ*-Induced Heterogeneous Grain Structure,'' *J. Am. Ceram. Soc.*, **77** [10] 2518–22 (1994).

[15]H. H. K. Xu, L. Wei, N. P. Padture, B. R. Lawn, and R. L. Yeckley, ''Effect of Microstructural Coarsening on Hertzian Contact Damage in Silicon Nitride,'' *J. Mater. Sci.*, **30,** 869–78 (1995).

[16]A. C. Fischer-Cripps and B. R. Lawn, ''Indentation Stress–Strain Curves for ''Quasi-Ductile'' Ceramics,'' *Acta Metall.*, **44** [2] 519–27 (1996).

[17]S. K. Lee, S. Wuttiphan, and B. R. Lawn, ''Role of Microstructure in Hertzian Contact Damage in Silicon Nitride: I, Mechanical Characterization,'' *J. Am. Ceram. Soc.*, **80** [9] 2367–81 (1997).

[18]S. K. Lee, K. S. Lee, B. R. Lawn, and D. K. Kim, ''Effect of Starting Powder on Damage Resistance of Silicon Nitrides,'' *J. Am. Ceram. Soc.*, in press.

[19]S. K. Lee and B. R. Lawn, ''Role of Microstructure in Hertzian Contact Damage in Silicon Nitride: II, Strength Degradation,'' *J. Am. Ceram. Soc.*, **81** [4] 997–1003 (1998).

[20]B. R. Lawn, N. P. Padture, F. Guiberteau, and H. Cai, ''A Model for Microcrack Initiation and Propagation Beneath Hertzian Contacts in Polycrystalline Ceramics,'' *Acta Metall.*, **42** [5] 1683–93 (1994).

[21]N. P. Padture and B. R. Lawn, ''Contact Fatigue of a Silicon Carbide with a Heterogeneous Grain Structure,'' *J. Am. Ceram. Soc.*, **78** [6] 1431–38 (1995).

[22]H. H. K. Xu, S. Jahanmir, L. K. Ives, L. S. Job, and K. T. Ritchie, ''Short-Crack Toughness and Abrasive Machining of Silicon Nitride,'' *J. Am. Ceram. Soc.*, **79** [12] 3055–64 (1996).

[23]N. P. Padture, C. J. Evans, H. H. K. Xu, and B. R. Lawn, ''Enhanced Machinability of Silicon Carbide via Microstructural Design,'' *J. Am. Ceram. Soc.*, **78** [1] 215–17 (1995).

[24]L. An, H. M. Chan, N. P. Padture, and B. R. Lawn, ''Damage-Resistant Alumina-Based Layer Composites,'' *J. Mater. Res.*, **11** [1] 204–10 (1996).

[25]S. Wuttiphan, B. R. Lawn, and N. P. Padture, ''Crack Suppression in Strongly-Bonded Homogeneous/Heterogeneous Laminates: A Study on Glass/Glass-Ceramic Bilayers,'' *J. Am. Ceram. Soc.*, **79** [3] 634–40 (1996).

[26]O. Prakash, P. Sarkar, and P. S. Nicholson, ''Crack Deflection in Ceramic/Ceramic Laminates with Strong Interfaces,'' *J. Am. Ceram. Soc.*, **78** [4] 1125–27 (1995).

[27]H. Wang and X.-Z. Hu, ''Surface Properties of Ceramic Laminates Fabricated by Die Pressing,'' *J. Am. Ceram. Soc.*, **79** [2] 553–56 (1996).

[28]K. S. Lee, S. Wuttiphan, X. Z. Hu, S. K. Lee, and B. R. Lawn, ''Contact-Induced Transverse Fractures in Brittle Layers on Soft Substrates: A Study on Silicon Nitride Bilayers,'' *J. Am. Ceram. Soc.*, **81** [3] 571–80 (1998).

[29]H. Liu and S. M. Hsu, ''Fracture Behavior of Multilayer Silicon Nitride/Boron Nitride Ceramics,'' *J. Am. Ceram. Soc.*, **79** [9] 2452–57 (1996).

[30]H. Liu, B. R. Lawn, and S. M. Hsu, ''Hertzian Contact Response of Tailored Silicon Nitride Multilayers,'' *J. Am. Ceram. Soc.*, **79** [4] 1009–14 (1996).

[31]D. B. Marshall and B. R. Lawn, ''An Indentation Technique for Measuring Stresses in Tempered Glass Surfaces,'' *J. Am. Ceram. Soc.*, **60** [1–2] 86–87 (1977).

[32]H. Cai, M. A. Stevens Kalceff and B. R. Lawn, ''Deformation and Fracture of Mica-Containing Glass-Ceramics in Hertzian Contacts,'' *J. Mater. Res.*, **9** [3] 762–70 (1994).

[33]F. Guiberteau, N. P. Padture, and B. R. Lawn, ''Effect of Grain Size on Hertzian Contact in Alumina,'' *J. Am. Ceram. Soc.*, **77** [7] 1825–31 (1994).

[34]B. R. Lawn, S. K. Lee, I. M. Peterson, and S. Wuttiphan, ''A Model of Strength Degradation from Hertzian Contact Damage in Tough Ceramics,'' *J. Am. Ceram. Soc.*, **81** [6] 1509–20 (1998).

[35]B. R. Lawn and D. B. Marshall, ''Nonlinear Stress–Strain Curves for Solids Containing Closed Cracks with Friction,'' *J. Mech. Phys. Solids*, **46** [1] 85–113 (1998).

[36]K. Komvopolous, ''Elastic–Plastic Finite Element Analysis of Indented Layered Media,'' *ASME J. Tribol.*, **111**, 430–39 (1989).

[37]A. Pajares, L. Wei, B. R. Lawn, N. P. Padture, and C. C. Berndt, ''Mechanical Characterization of Plasma-Sprayed Ceramic Coatings on Metal Substrates by Contact Testing,'' *Mater. Sci. Eng.*, **A208** [2] 158–65 (1996).

[38]A. Pajares, L. Wei, B. R. Lawn, and C. C. Berndt, ''Contact Damage in Plasma-Sprayed Alumina-Based Coatings,'' *J. Am. Ceram. Soc.*, **79** [7] 1907–14 (1996).

[39]S. Timoshenko and J. N. Goodier, *Theory of Elasticity.* McGraw-Hill, New York, 1951.

[40]L. M. Braun, S. J. Bennison, and B. R. Lawn, ''Objective Evaluation of Short-Crack Toughness-Curves Using Indentation Flaws: Case Study on Alumina-Based Ceramics,'' *J. Am. Ceram. Soc.*, **75** [11] 3049–57 (1992).

[41]W. C. Young, *Roark's Formulas for Stress and Strain*; pp. 118–19. McGraw-Hill, New York, 1989.

[42]B. R. Lawn, S. M. Wiederhorn, and H. Johnson, ''Strength Degradation of Brittle Surfaces: Blunt Indenters,'' *J. Am. Ceram. Soc.*, **58** [9–10] 428–32 (1975). □